


 Cite this: *RSC Adv.*, 2021, **11**, 24747

A class of novel luminescent layered double hydroxide nanotubes[†]

Dimy Nanclares, Alysson F. Morais, * Thainá Calaça, Ivan G. N. Silva and Danilo Mustafa

Herein, we report a class of novel lanthanide-doped self-supported layered double hydroxide (LDH) nanotubes featuring a combination of micro- and mesoporosity. The synthesis of the nanotubes has been achieved by a soft-templating strategy. Incorporation of La^{3+} , Pr^{3+} , Nd^{3+} , Sm^{3+} , Eu^{3+} , Gd^{3+} or Tb^{3+} in the LDHs assisted the self-assembly of the double hydroxide layers onto the surface of Pluronic P-123 worm-like micelles, enabling the formation of the nanotubes. Removal of the micellar template provides accessibility to the mesopores, yielding a network of hollow cylindrical nanotubes with internal diameter of about 10 nm. An antenna molecule (benzene-1,3,5-tricarboxylate, BTC) is hosted in their 1-nanometre-wide micropores. Upon UV excitation, the nanotubes emit light in a set of wavelengths ranging from the ultraviolet to the infrared.

 Received 20th May 2021
 Accepted 8th July 2021

 DOI: 10.1039/d1ra03948b
rsc.li/rsc-advances

Introduction

To address the high demand for new functional materials from fields such as catalysis, separation science, chromatography, gas storage and sensing, major efforts have been invested in the development of new hierarchically porous materials with tunable composition, pore size and chemical functionality.^{1–5} Layered double hydroxides (LDHs) are intrinsically microporous anion exchange matrices related to the sheet mineral brucite – $\text{Mg}(\text{OH})_2$. Equimolar substitution of the divalent metal cations (M^{II}) in $\text{M}^{\text{II}}(\text{OH})_2$ brucite-like layers by trivalent elements (M^{III}) yields positively charged $[\text{M}_{1-z}^{\text{II}}\text{M}_z^{\text{III}}(\text{OH})_2]^{z+}$ lamellae. Neutral LDH solids are formed by the stacking of these hydroxide sheets with hydrated anions ($\text{A}^{n-} \cdot \text{yH}_2\text{O}$), leading to the general chemical formula $[\text{M}_{1-z}^{\text{II}}\text{M}_z^{\text{III}}(\text{OH})_2]^{z+}[\text{A}^{n-}]^{z/n} \cdot \text{yH}_2\text{O}$. A wide set of polyvalent metals and anions can be introduced, respectively, in the hydroxide layers and in the interlayer gallery of LDHs, making the physico-chemical properties of these synthetic minerals tunable towards the desired application. Owing to this flexibility, LDHs have been successfully applied as solid electrolytes, catalysts, adsorbents and drug delivery vectors.^{6–13}

In regard to the porous structure of LDHs, they are typically microporous solids that exhibit low specific surface area. Nanostructuring is a promising route to increase the specific surface area of LDHs.¹⁴ In addition, the combination of micro-

and mesoporosity in hierarchical 3D morphologies should lead to LDHs with improved diffusional and adsorptive properties. Development of novel hierarchical LDH nanoparticles featuring large and accessible mesopores could provide interesting opportunities in catalysis and nanomedicine.^{15,16}

Carbon nanotubes, NiCo_2O_4 nanowires and Fe_3O_4 microspheres have successfully been used to produce hard template-supported LDH nanoparticles.^{17–20} While these formulations successfully yielded 3D nanostructures, the presence of the support blocks mesopore accessibility. To date, only a few self-supported hierarchical LDHs structures have been reported, with the production of nanospheres, microspheres, nanocones and nanoscrolls.^{21–24} Production of self-supported LDH nanoparticles with accessible mesopores could be within reach by using soft templating methods to induce the self-assembly of the double hydroxides layers onto the soft-template surface. A mesoporous structure would be obtained after removal of the structure directing agent. However, employing soft templating to produce mesoporous LDH nanoparticles involves some challenges. Within the hydroxide layers of LDHs, the metal cations are typically octahedrally coordinated. The close packing of these octahedral units yields a flat 2D layer with high rigidity with respect to transverse distortions and curvature.²⁵ Thus, without the introduction of defects in the hydroxide layers, template methods aiming at inducing a 3D hierarchical morphology on LDHs tend to fail. On the other hand, it is well known that in layered rare earth hydroxides (LREH), which are layered materials related to the LDHs, a sinusoidal wave-like topology develops from the non-octahedral coordination of the rare earth elements.^{26,27} Inspired on this, we addressed the challenge of imposing a 3D hierarchical morphology on LDHs by introducing triply charged lanthanide ions (Ln^{3+}) in the

Instituto de Física, Universidade de São Paulo, São Paulo/SP, Brazil. E-mail: alyssonfmorais@gmail.com; Tel: +55 11 3091 6879

[†] Electronic supplementary information (ESI) available: Synthesis and characterization of new compounds, X-ray diffraction, electron micrographs, photoluminescence spectroscopy and thermogravimetric curves. See DOI: 10.1039/d1ra03948b



hydroxide layers of LDHs ($\text{ZnAlLn}_{X\%}\text{-BTC-P123}$, X denoting the substitution fraction $\text{Ln}/(\text{Ln} + \text{Al})$). Inclusion of this non-octahedral site in the LDH structure enabled the curvature of the LDH sheets, unlocking the possibility of using a soft-templating strategy to produce a class of novel hierarchical LDH nanotubes.^{28–31} Pluronic® P-123 worm-like micelles were used as structure directing agents. Among the lanthanides, La^{3+} , Pr^{3+} , Nd^{3+} , Sm^{3+} , Eu^{3+} , Gd^{3+} and Tb^{3+} were observed to induce the formation of the nanotubes. Contrastingly, inclusion of the smaller lanthanides Dy^{3+} , Ho^{3+} , Er^{3+} , Tm^{3+} , Yb^{3+} and Lu^{3+} in the LDH structure still produced platy-like LDH crystals. In the interlayer gallery, the LDH nanotubes host an antenna molecule (benzene-1,3,5-tricarboxylate, BTC), responsible to absorb UV radiation and transfer to the lanthanides.³² Upon UV excitation, the nanotubes emit light in a set of wavelengths ranging from the ultraviolet to the infrared.

In a typical synthetic procedure, $\text{ZnAlLn}_{X\%}\text{-BTC-P123}$ hollow nanotubes singly doped with a lanthanide ion (Ln^{3+}) were produced as follows. Pluronic P-123 worm-like micelles were synthesized by dissolving BTC (11.5×10^{-3} mol L⁻¹) and P-123 (0.15 wt%) in deionized water (200 mL) at 60 °C. After cooling down the solution to room temperature, a second heating cycle to 60 °C was done in order to optimize micellization. The LDHs were prepared by slowly dosing (10 mL h⁻¹) a 10 millilitres-solution containing $\text{Zn}(\text{NO}_3)_2 \cdot 6\text{H}_2\text{O}$, $\text{Al}(\text{NO}_3)_3 \cdot 9\text{H}_2\text{O}$ and $\text{Ln}(\text{NO}_3)_3 \cdot 6\text{H}_2\text{O}$ in the stoichiometric ratio $2 : 1 - X : X$ and at a total metal concentration of 1 mol L⁻¹ into the solution containing the micelles. The pH of the mother solution was stated to pH 8 by a Metrohm 848 Titroplus automatic titrator. After the metal solution has been completely dosed, the resulting slurry was recovered by centrifugation. Removal of the polymeric structure-directing agent was accomplished by liquid extraction with methanol in ultrasonically agitated bath (confirmed by thermogravimetric analysis, Fig. S1†). The detailed synthetic and characterization procedures are provided in the ESI.†

Results and discussion

The PXRD patterns of the $\text{ZnAlLn}_{5\%}\text{-BTC-P123}$ LDHs are displayed in Fig. 1 (for La and from Nd to Er) and Fig. S2A† (for Pr and from Ho to Lu). The Bragg reflections were indexed based on a 3-layer hexagonal unit cell. The (003) basal peak at around 6.7° 2θ directly relates to the basal spacing of the LDHs (see Table S1†). Discounting the typical thickness of the hydroxide layers (~0.48 nm) the average interlayer distance can be calculated to be around 0.84 nm. This is compatible with the longitudinal size of BTC and indicates the presence of this anion in the interlayer gallery with an orientation transverse to the hydroxide layers.^{32,33} In the region from 58° to 62° 2θ, the Ln^{3+} -substituted LDHs present a broad diffraction peak formed by the (110) and (113) Bragg reflections. From the position of this broad feature, the average metal–metal distance (d_{MM}) within the LDH sheets can be estimated as: $d_{\text{MM}} = 2d_{(110)} \sim 0.304$ nm (see Table S1†).

Compared to Ln^{3+} -free ZnAl-BTC-P123 LDHs, the basal reflections for $\text{ZnAlLn}_{5\%}\text{-BTC-P123}$ are broadened (see Table S1†).

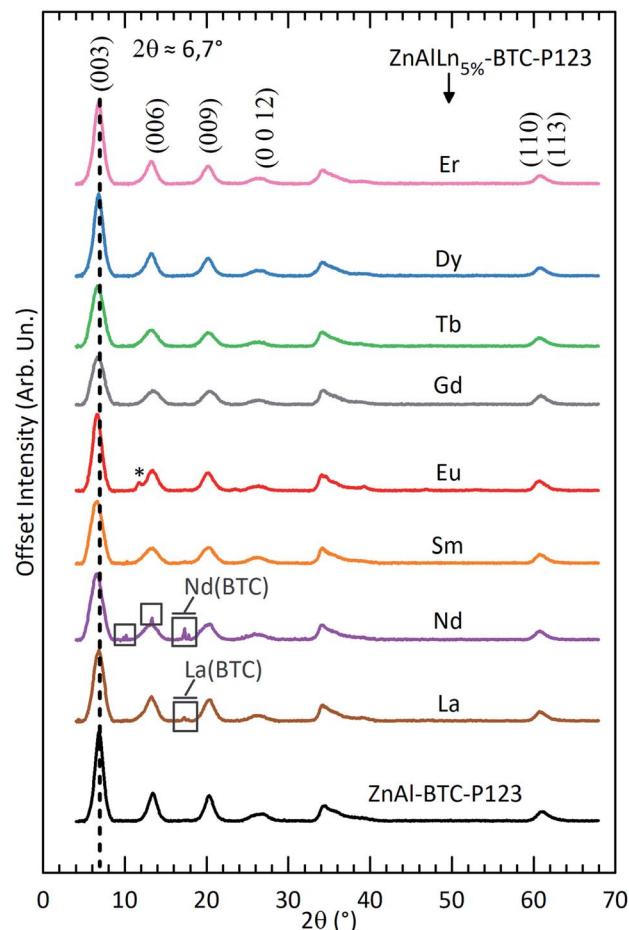


Fig. 1 Powder X-ray diffraction patterns of ZnAl-BTC-P123 and $\text{ZnAlLn}_{5\%}\text{-BTC-P123}$ ($\text{Ln} = \text{La}$ and from Nd to Er). The Bragg peaks inside the rectangles are attributed to the formation of the respective $\text{Ln}(\text{BTC})$ complex.^{35–37} The starred peak are ascribed to a carbonate-intercalated LDH phase formed in the Eu^{3+} -containing solid.

This broadening accounts to the distortions caused in the hydroxide layers by the heteromorphous substitution of Al^{3+} and Zn^{2+} by the lanthanides. Also contributing to this broadening is the decrease in crystallite size caused by the introduction of lanthanides in the LDH sheets, as has been already observed in previous investigations.³⁴

While the formation constant of the Ln -benzenecarboxylate complexes is kept almost unchanged over the lanthanides, the solubility constant of their hydroxide phases decreases along the lanthanide series.^{38,39} The combination of these two features explains the here observed trend that the limit Ln^{3+} concentration for which only a pure LDH phase is formed increases along the lanthanide series, as shown by PXRD. In fact, lanthanum hydroxide has the highest solubility constant over the lanthanides. Formation of the $\text{La}(\text{BTC})$ complex is observed already with a 3% substitution fraction (Fig. S2B†). On the other hand, no complex formation was observed in the Lu^{3+} -containing solids up to $X = 15\%$ (Fig. S2C†).

The morphology of the Ln -containing LDH particles was characterized by transmission electron microscopy



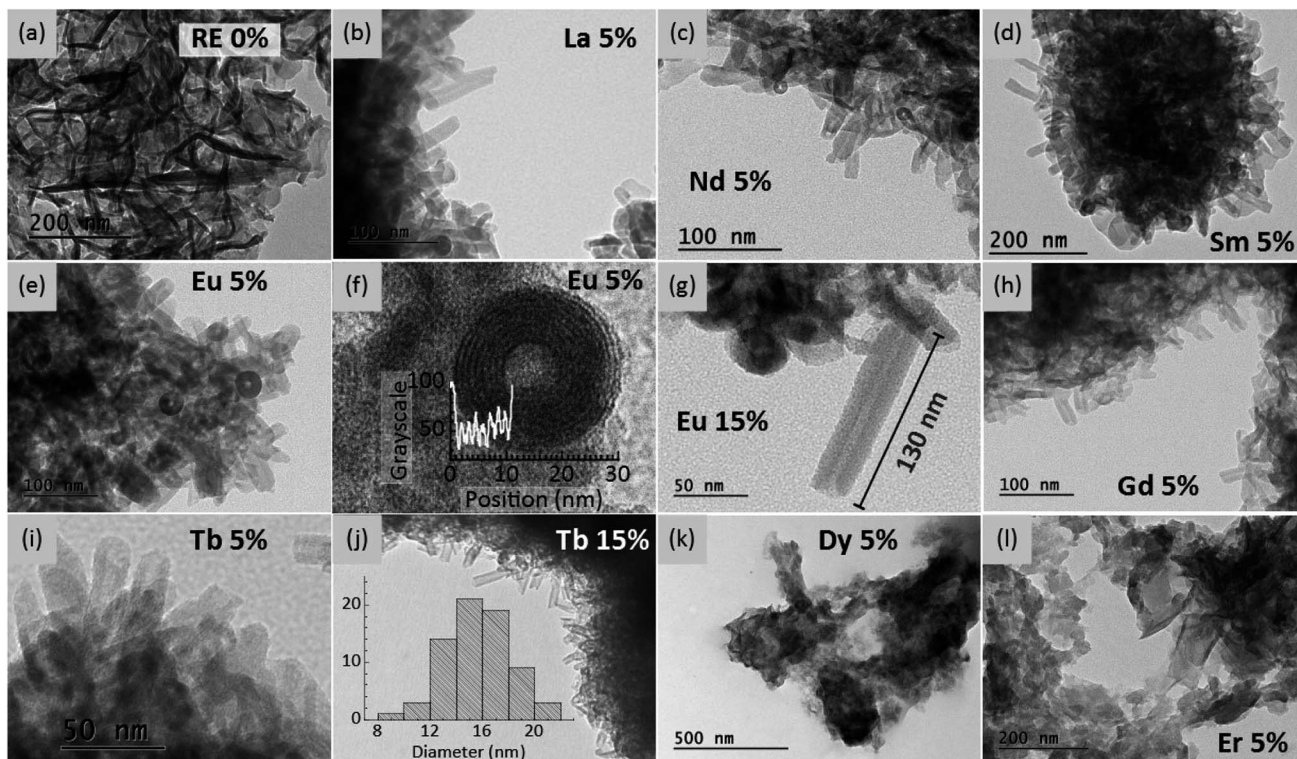


Fig. 2 Transmission electron micrographs comparing the morphology of (a) ZnAl–BTC and (b–l) ZnAlLn_X%–BTC–P123 (Ln = La and from Nd to Er, X = 5 or 15%). The pixel profile along the diameter of a nanotube is shown on (f). The inset in (j) displays the external diameter distribution histogram of the ZnAlTb₁₅%–BTC–P123 nanotubes.

(Fig. 2 and S3†). Without incorporation of lanthanides (ZnAl–BTC–P123, Fig. 2a) only flake-like LDH crystals are formed. For Tb³⁺ and the other lanthanides with larger ionic radius (La to Tb), the combination of Ln³⁺, BTC and P-123 worm-like micelles produced well defined LDH nanotubes with typical external diameter of 16 nm (inset of Fig. 2j). Contrastingly, introduction of the smaller lanthanides Dy³⁺, Ho³⁺, Er³⁺, Tm³⁺, Yb³⁺ and Lu³⁺ only yielded plate-like LDHs. Interestingly, a similar feature has been observed for LREH, for which a high coordination number for the metal sites is needed to stabilize the sinusoidal topology of these layered structures.^{27,40} On this basis, the decrease in coordination capacity along the lanthanide series hinders the formation of these materials. Here, the same explanation can be used to speculate on the role of the lanthanides in the self-assembly of the nanotubes: one can tentatively explain the formation of these self-supported 3D structures by the increased stability of a bent LDH sheet containing non-octahedral metal sites with high coordination number. Within this hypothesis, the high coordination capacity of the larger Ln³⁺ ions enables the hydroxide layers to accommodate the curvature necessary for the formation of the nanotubes.

Aside to assisting the mesostructuring of the LDHs, doping different lanthanides into the hydroxide layers renders these materials photoluminescent.⁴¹ Most remarkable are the pinkish, reddish, greenish and bluish PL of Sm³⁺, Eu³⁺, Tb³⁺ and Dy³⁺,

respectively (see Fig. 3). The emission and excitation spectra of the LDH samples are shown in Fig. S4.†

The pinkish emission of the Sm³⁺-substituted LDHs nanotubes arises from the combination of the characteristic orange emission of Sm³⁺ with a relevant contribution from the violaceous fluorescence of BTC. The Sm³⁺ 4f–4f emission bands (Fig. S4A†) are mainly located in the visible region and correspond to the (J + 1/2) Stark components of the $^4G_{5/2} \rightarrow ^6H_{J/2}$ (J = 5, 7, 9 or 11) intraconfigurational electronic transitions with wavelengths centered at 563.8 nm, 599.4 nm, 645.8 nm and 706.8 nm, respectively. In the excitation spectrum of the Sm³⁺-containing nanotubes, the excitation bands are assigned to transitions from the $^6H_{5/2}$ ground state to the following excited levels of Sm³⁺ (barycentre in cm^{-1}): $^4H_{9/2}$ (29 085), $^4D_{3/2}$ (27 599), $^6P_{7/2}$ (26 801), $^6P_{3/2}$, $^4L_{13/2}$ (24 850), $^6P_{5/2}$ (23 964), $^4I_{13/2}$ (21 632). Additionally, the broad and most intense band below

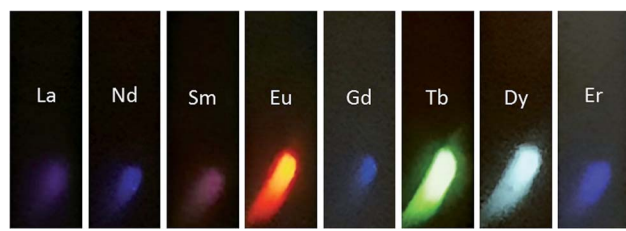


Fig. 3 Pictures of ZnAlRE₅%–BTC–P123 samples exposed to UV radiation (290 nm).



380 nm is ascribed to the $S_0(\pi) \rightarrow S_n(^1\pi^*)$ singlet–singlet absorption of BTC with posterior energy transfer to Sm^{3+} . The high intensity of this ligand-to-metal excitation band as compared to the direct excitation bands of Samarium shows that BTC works as an efficient antenna molecule in this system.

The photoluminescence and absorption spectra of the Eu^{3+} -containing nanotubes are displayed on Fig. S4B.† The excitation spectrum obtained by monitoring the $(\text{Eu}^{3+})^5\text{D}_0 \rightarrow {}^7\text{F}_2$ hypersensitive transition at 614 nm features a broad and intense band from 240 to 350 nm, ascribed to the $S_0(\pi) \rightarrow S_n(^1\pi^*)$ transition of BTC. The sharp bands arising from direct excitation of the $(\text{Eu}^{3+})^7\text{F}_{0,1} \rightarrow {}^5\text{L}_6$ and $(\text{Eu}^{3+})^7\text{F}_{0,1} \rightarrow {}^5\text{D}_2$ 4f–4f intraconfigurational transitions of Eu^{3+} are also visible at 394.3 and 464.7 nm, respectively. In the emission spectrum, the $(\text{Eu}^{3+})^5\text{D}_0 \rightarrow {}^7\text{F}_{0-6}$ emission bands are visible. The Eu^{3+} -containing LDH nanotubes feature a characteristic red PL under UV excitation which is dominated by the $(\text{Eu}^{3+})^5\text{D}_0 \rightarrow {}^7\text{F}_2$ hypersensitive transition. As the $(\text{Eu}^{3+})^5\text{D}_0 \rightarrow {}^7\text{F}_2$ and $(\text{Eu}^{3+})^5\text{D}_0 \rightarrow {}^7\text{F}_4$ emissions are much more intense than the $(\text{Eu}^{3+})^5\text{D}_0 \rightarrow {}^7\text{F}_1$, it is mostly likely that the lanthanide ions in the hydroxide layers are hosted in a site with no inversion symmetry.⁴² This clearly rules out the octahedral symmetry commonly observed for the metal sites in LDHs and further indicate that the inclusion of the lanthanides in these materials distorts the hydroxide layers.

The photoluminescence (PL) of the Tb-containing LDH nanotubes (Fig. S4C†) is dominated by the $(\text{Tb}^{3+})^5\text{D}_4 \rightarrow {}^7\text{F}_5$ emission, which confers the greenish PL of this material. All $(\text{Tb}^{3+})^5\text{D}_4 \rightarrow {}^7\text{F}_J$ ($J = 0-6$) emissions are visible, respectively at 488.9, 542.5, 584.4, 622.2, 647.8, 671.0 and 681.6 nm. Given the very high ligand-to-metal excitation band observed in the excitation spectrum of $\text{ZnAlTb}_{5\%}\text{-BTC-P123}$, the excitation bands of the Tb^{3+} activators are not discernible, which shows that BTC works as an excellent antenna in the Tb-containing nanotubes, giving rise to samples with very bright PL under UV excitation (Fig. 3). In fact, the energy of the Tb^{3+} emitting level (${}^5\text{D}_4$, $\sim 20\ 440\ \text{cm}^{-1}$) is resonant with the $\text{T}_1(^3\pi^*)$ band of BTC (\sim from 18 600 to 25 000 cm^{-1}), which facilitates intersystem energy transfer.

The emission spectrum of platy-like LDHs $\text{ZnAlDy}_{5\%}\text{-BTC-P123}$ is given in Fig. S4D.† The $(\text{Dy}^{3+})^4\text{F}_{9/2} \rightarrow {}^6\text{H}_J$ ($J = 15, 13, 11, 9$ or 7) intraconfigurational transitions are observed at, respectively, 480.8, 574.4, 663.8, 751.7 and 835.0 nm. The ligand-to-metal energy transfer band with promotion of the $S_0(\pi) \rightarrow S_n(^1\pi^*)$ singlet–singlet transition of BTC dominates the excitation spectrum indicating an efficient sensitization of Dy^{3+} , which features a bright bluish PL under UV excitation.

A violaceous PL is observed for the La-, Nd-, Gd- and Er-containing LDHs, attributed to the fluorescence of BTC in the UV/violet region (Fig. S5†). BTC fluorescence is observable either due to the lack of an efficient ligand-to-metal energy transfer route (the case for the La- and Gd-containing materials) or due to luminescence quenching in systems containing the narrow band gap lanthanides Nd^{3+} and Er^{3+} . In fact, for La^{3+} , an element with an empty 4f shell, no BTC-to-La energy transfer can occur, making light emission from BTC more likely to occur. Also, Gd^{3+} is a half-full 4f shell metal featuring a wide energy band gap ($\sim 32\ 200\ \text{cm}^{-1}$) between the ${}^8\text{S}_{7/2}$ ground state

and the ${}^6\text{P}_{7/2}$ first excited level.⁴³ The $(\text{Gd}^{3+})^6\text{P}_{7/2}$ level is far above the triplet levels of BTC, making that no ligand-to-metal energy transfer can occur.⁴⁴

Conclusions

Introduction of large lanthanide sites in LDHs assisted the self-assembly of self-supported LDH nanotubes featuring a combination of micro- and mesoporosity. Synthesis of nanotubes containing La^{3+} , Pr^{3+} , Nd^{3+} , Sm^{3+} , Eu^{3+} , Gd^{3+} or Tb^{3+} was accomplished by a soft templating strategy with the use of Pluronic P-123 worm-like micelles as structure directing agents. Not all the elements in the lanthanide series yielded nanotubes, with the inclusion of the smaller cations Dy^{3+} , Ho^{3+} , Er^{3+} , Tm^{3+} , Yb^{3+} and Lu^{3+} in the double hydroxide layers still producing platy-like LDH crystals. This indicates that the inclusion of sites with high coordination number in the LDHs is key to unlock the possibility of using soft templating strategies to produce novel 3D LDH morphologies.

Author contributions

DN: investigation, data curation, formal analysis and writing – original draft. AFM: conceptualization, methodology, formal analysis, data validation, writing – original draft and writing – review & editing. TC: investigation (La^{3+} , Dy^{3+} and Tm^{3+} -containing samples). IGNS: conceptualization, supervision and writing – review and editing. DM: conceptualization, project administration, funding acquisition and supervision. All authors discussed the results and revised the manuscript.

Conflicts of interest

There are no conflicts to declare.

Acknowledgements

The authors acknowledge the Laboratory of Crystallography (IFUSP, São Paulo) for assistance with the PXRD measurements and Alfredo Duarte (Central Analítica – IQUSP, São Paulo) for assistance with the TEM measurements. This research was funded by Fundação de Amparo à Pesquisa do Estado de São Paulo (FAPESP, 2015/19210-0 and 2018/13837-0), Coordenação de Aperfeiçoamento de Pessoal de Nível Superior (CAPES, 1723707, Finance Code 001) and Conselho Nacional de Desenvolvimento Científico e Tecnológico (CNPq, 142127/2014-0, 403055/2016-4 and 140196/2017-0).

References

- 1 X.-Y. Yang, L.-H. Chen, Y. Li, J. C. Rooke, C. Sanchez and B.-L. Su, *Chem. Soc. Rev.*, 2017, **46**, 481–558.
- 2 M.-H. Sun, S.-Z. Huang, L.-H. Chen, Y. Li, X.-Y. Yang, Z.-Y. Yuan and B.-L. Su, *Chem. Soc. Rev.*, 2016, **45**, 3479–3563.
- 3 Y. Zhong, G. Chen, X. Liu, D. Zhang, N. Zhang, J. Li, S. Liang, R. Ma and G. Qiu, *Nanoscale*, 2017, **9**, 8185–8191.



4 H. Wang, Z. Sun, X. Zou, J. Ren and C. Zhang, *Nanoscale*, 2021, **13**, 6241–6247.

5 C. Perego and R. Millini, *Chem. Soc. Rev.*, 2014, **42**, 3956–3976.

6 A. I. Khan and D. O'Hare, *J. Mater. Chem.*, 2002, **12**, 3191–3198.

7 G. Fan, F. Li, D. G. Evans and X. Duan, *Chem. Soc. Rev.*, 2014, **43**, 7040–7066.

8 R. Santos, J. Tronto, V. Briois and C. Santilli, *J. Mater. Chem. A*, 2017, **5**, 9998–10009.

9 S. Zhang, F. Yao, L. Yang, F. Zhang and S. Xu, *Carbon*, 2015, **93**, 143–150.

10 L. Mohapatra and K. Parida, *J. Mater. Chem. A*, 2016, **4**, 10744–10766.

11 A. Khenifi, Z. Derriche, C. Mousty, V. Prévot and C. Forano, *Appl. Clay Sci.*, 2010, **47**, 362–371.

12 K. Ladewig, Z. P. Xu and G. Q. M. Lu, *Expert Opin. Drug Delivery*, 2009, **6**, 907–922.

13 X. Bi, H. Zhang and L. Dou, *Pharmaceutics*, 2014, **6**, 298–332.

14 Y. Zhao, G. Chen, T. Bian, C. Zhou, G. I. N. Waterhouse, L. Wu, C. Tung, L. J. Smith, D. O'Hare and T. Zhang, *Adv. Mater.*, 2015, **27**, 7824–7831.

15 Y. Li, D. Liu, H. Ai, Q. Chang, D. Liu, Y. Xia, S. Liu, N. Peng, Z. Xi and X. Yang, *Nanotechnology*, 2010, **21**, 105101.

16 S. Li, J. Li, C. J. Wang, Q. Wang, M. Z. Cader, J. Lu, D. G. Evans, X. Duan and D. O'Hare, *J. Mater. Chem. B*, 2013, **1**, 61–68.

17 X. Chen, F. Mi, H. Zhang and H. Zhang, *Mater. Lett.*, 2012, **69**, 48–51.

18 L. Li, Y. Feng, Y. Li, W. Zhao and J. Shi, *Angew. Chem., Int. Ed.*, 2009, **48**, 5888–5892.

19 L. Huang, D. Chen, Y. Ding, S. Feng, Z. L. Wang and M. Liu, *Nano Lett.*, 2013, **13**, 3135–3139.

20 J. Zhao, J. Chen, S. Xu, M. Shao, Q. Zhang, F. Wei, J. Ma, M. Wei, D. G. Evans and X. Duan, *Adv. Funct. Mater.*, 2014, **24**, 2938–2946.

21 X. Liu, R. Ma, Y. Bando and T. Sasaki, *Adv. Mater.*, 2012, **24**, 2148–2153.

22 L. Li, R. Ma, N. Iyi, Y. Ebina, K. Takada and T. Sasaki, *Chem. Commun.*, 2006, 3125–3127.

23 M. A. Rocha, P. A. Petersen, E. Teixeira-Neto, H. M. Petrilli, F. Leroux, C. Taviot-Gueho and V. R. Constantino, *RSC Adv.*, 2016, **6**, 16419–16436.

24 M. Shao, F. Ning, Y. Zhao, J. Zhao, M. Wei, D. G. Evans and X. Duan, *Chem. Mater.*, 2012, **24**, 1192–1197.

25 M. Thorpe and S. Solin, *Access in Nanoporous Materials*, Springer, 2002, pp. 59–71.

26 R. Ma and T. Sasaki, *Adv. Mater.*, 2010, **22**, 5082–5104.

27 J. Liang, R. Ma and T. Sasaki, *Dalton Trans.*, 2014, **43**, 10355–10364.

28 A. F. Morais, I. G. Silva, S. P. Sree, F. M. de Melo, G. Brabants, H. F. Brito, J. A. Martens, H. E. Toma, C. E. Kirschhock, E. Breynaert, *et al.*, *Chem. Commun.*, 2017, **53**, 7341–7344.

29 I. G. N. Silva, A. F. Morais, B. C. Lima, F. A. Garcia and D. Mustafa, *Appl. Clay Sci.*, 2020, **199**, 105861.

30 A. F. Morais, I. G. N. Silva, B. C. Lima, F. A. Garcia and D. Mustafa, *ACS Omega*, 2020, **5**, 23778–23785.

31 A. F. Morais, D. Nanclares, I. G. N. Silva, A. Duarte, F. A. Garcia, E. Breynaert and D. Mustafa, *Nanoscale*, 2021, DOI: 10.1039/D1NR02477A.

32 A. F. Morais, F. O. Machado, A. C. Teixeira, I. G. N. Silva, E. Breynaert and D. Mustafa, *J. Alloys Compd.*, 2019, **771**, 578–583.

33 B. Shao, P. Feng, X. Wang, F. Cui and X. Yang, *J. Phys. Chem. C*, 2019, **123**, 7467–7474.

34 A. W. Musumeci, Z. P. Xu, S. V. Smith, R. F. Minchin and D. J. Martin, *J. Nanopart. Res.*, 2010, **12**, 111–120.

35 I. G. Silva, D. Mustafa, B. Andreoli, M. C. Felinto, O. L. Malta and H. F. Brito, *J. Lumin.*, 2016, **170**, 364–368.

36 C. Daiguebonne, O. Guilloa, Y. Géralt, A. Lecerf and K. Boubekeur, *Inorg. Chim. Acta*, 1999, **284**, 139–145.

37 C. Serre, F. Millange, C. Thouvenot, N. Gardant, F. Pellé and G. Férey, *J. Mater. Chem.*, 2004, **14**, 1540–1543.

38 G. R. Choppin, P. A. Bertrand, Y. Hasegawa and E. N. Rizkalla, *Inorg. Chem.*, 1982, **21**, 3722–3724.

39 P. L. Brown and C. Ekberg, *Hydrolysis of Metal Ions - Chap 6: Scandium, Yttrium and the Lanthanide Metals*, Wiley, 2016.

40 B. Shao, P. Feng, X. Wang, F. Cui and X. Yang, *J. Phys. Chem. C*, 2019, **123**, 7467–7474.

41 A. W. Musumeci, Z. P. Xu, S. V. Smith, R. F. Minchin and D. J. Martin, *J. Nanopart. Res.*, 2010, **12**, 111–120.

42 K. Binnemans, *Coord. Chem. Rev.*, 2015, **295**, 1–45.

43 P. S. Peijzel, P. Vermeulen, W. J. M. Schrama, A. Meijerink, M. F. Reid and G. W. Burdick, *Phys. Rev. B*, 2005, **71**, 125126.

44 E. R. Souza, I. G. Silva, E. E. Teotonio, M. C. Felinto and H. F. Brito, *J. Lumin.*, 2010, **130**, 283–291.

